A Semi-Analytic Model of Fog Effects on Vision

Eric Dumont[1], Nicolas Hautière[1], Romain Gallen[1,2]

[1] Laboratoire Central des Ponts et Chaussées,
Division Exploitation Signalisation Eclairage,
58 boulevard Lefebvre, 75015 Paris, France

[2] Laboratoire sur les Interactions Véhicules Infrastructure Conducteurs,
unité mixte de l'INRETS et du LCPC,
bâtiment 824, 14 route de la Minière, 78000 Versailles, France

Abstract - Fog is often considered as a mere nuisance rather than a hazard. However, reduced meteorological visibility conditions cause accidents and transportation delays, with substantial financial consequences. The visibility loss results from minute airborne droplets which scatter light, causing drastic alterations in the image of the environment perceived by vision systems, both human and artificial. Modeling the visual effects of dense fog makes it possible to simulate foggy conditions, in order to design and test countermeasures for improved safety and mobility. First, we introduce basic notions about the nature of fog and we briefly review the microphysical models which usually serve to describe its droplet size distribution. Second, we explain how light interacts with fog droplets, and we present the optical descriptors which describe scattering and extinction phenomena. Third, we analyze how contrast is impaired by these phenomena in the image of the environment perceived by a vision system, and we propose and discuss a semi-analytic model of the visual effects of fog. Finally, we show applications of this model to the monitoring of the meteorological visibility through use of charge-coupled device cameras operating in the visible light range.

1 Introduction

Dense fog drastically impairs visibility, causing important traffic safety issues, particularly in the field of ground transportation. In order to design and assess solutions for detecting and counterbalancing the loss of visual information in foggy weather conditions, the use of simulation can hardly be avoided, since field experiments are made very difficult by the lack of control over the time and place where fog will occur.

Two approaches are possible for simulating the image of a scene observed in fog: computer graphics and image processing. The first consists in simulating all radiative transfers between emitting and reflecting surfaces, taking into account the interactions with the participating medium [34]. It involves global illumination calculations which are generally

time-consuming. The other approach consists in simulating the perturbations caused in the image of the environment by the interactions of light with the scattering medium [7]. Originally designed for remote sensing, this approach has only recently found applications for horizontal visibility problems because of the depth-dependency of fog visual effects [29, 35].

This chapter shows how fog effects on vision can be simulated by image processing through a combination of depth-dependent (2D1/2) operations. First, we examine the nature and origin of fog, and we introduce its microphysical characteristics. Secondly, we consider the optical interactions between visible light and fog droplets, and we present the optical parameters characterizing the scattering phenomenon. Then we analyze the distance-dependent effects of light scattering on human or camera vision, and we propose a unified photometric model for simulating foggy weather conditions by image processing. Finally, we show applications of the model to the monitoring of the meteorological visibility through use of charge-coupled device cameras operating in the visible light range.

2 Fog Nature and Microstructure

2.1 Meteorological Phenomenon

The atmosphere always contains some concentration of sub-micron hygroscopic particles, with higher quantities in polluted areas (smoke, dust) or sea coasts (salt). These particles serve as condensation nuclei and support the condensation of water vapor when the air temperature approaches dew point. This may happen in two ways: either as the air cools or as the humidity rises. The most stable fogs are those which are caused by an inversion of temperature between the air and the ground. Such conditions usually lead to the formation of radiation or advection fog.

- Radiation fog (sometimes called ground fog) is the most common type of fog. It usually happens in late fall or early winter, when the land cools by thermal radiation after sunset, in calm conditions with clear sky.
- Advection fog happens when moist air moves over a cooler surface. It often happens when a cold marine layer is pushed or drawn to the coastline.

There are other types of fog, more localized or less stable, such as valley fog (which is essentially a confined radiation fog), evaporation or steam fog (caused by cold air standing over warm water or moist land), upslope fog (caused by moist air cooling as it is pushed upslope by the wind) or ice fog (which only occurs at extremely low temperatures). Fog is usually classified after the mechanism which lead to its formation, but it should be noted that several mechanisms may actually work simultaneously in the process.

Fog often dissipates naturally at sunrise, as the ground warms up, or when turbulences lift it and break it up into clouds. It may also be caused to break up artificially. Spreading salt or ice crystals, depending on the temperature, causes fog droplets to transform into raindrops or snowflakes, and forces their precipitation. Only large airports can afford this

technique, because it is not cost-effective: it only works in certain conditions, and there is no guaranty that fog will not reappear later on.

2.2 Fog Microstructure

Dispersed media may contain various sorts of solid or liquid particles, characterized by their numbers, their sizes, their shapes, and in some complex cases by their orientations, their chemical compositions and their structures [23]. Fog contains both water droplets formed around condensation nuclei and non-active sub-micron particles, but the latter have relatively little effect on light propagation. Therefore, fog is ordinarily assumed to contain spherical water droplets in different numbers and sizes [24, 36, 37].

2.2.1 Particle Size Distribution

Fog microstructure is characterized by a particle size distribution $n(r) = \mathrm{d}N(r)/\mathrm{d}r$, where $N(r)$ is the number of water droplets with a radius between r and $r + \mathrm{d}r$ per unit volume.

The droplet size distribution of fog has been observed to be unimodal [22]. It is generally characterized by the mode radius r_m, but other granulometric descriptors such as the mean radius $\bar{r}$, the effective radius r_e and the standard deviation σ are often used. Disperse media with different particle size distributions but identical effective radii and standard deviations are considered optically equivalent [23].

$$\bar{r} = \int_0^\infty r\, n(r)\, \mathrm{d}r \tag{1a}$$

$$r_\mathrm{e} = \frac{\int_0^\infty r^3\, n(r)\, \mathrm{d}r}{\int_0^\infty r^2\, n(r)\, \mathrm{d}r} \tag{1b}$$

$$\sigma = \sqrt{\int_0^\infty (r - \bar{r})^2\, n(r)\, \mathrm{d}r} \tag{1c}$$

2.2.2 Fog Granulometry

Theoretically, fog is in the same category of aerosols as clouds, with particle sizes between 2 and 50 μm [22]. In reality, different types of fog have different particle size distributions which evolve during their life-cycle [12]. According to Shettle and Fenn [36], who refer to several granulometric measurement campaigns, developing fogs contain 100 and 200 particles per cm^3 in the 1 to 10 μm radius range with mean radius of 2 to 4 μm, but as fog thickens droplet concentration may fall under 2 particles per cm^3 while the mean radius increases from 6 to 12 μm. More recent measurements reported by Guédalia and Bergot [14] seem to agree with these observations.

2.2.3 Granulometric Models

Measurements in natural fog are extremely difficult, mainly because it is almost impossible to ensure repeatable thermodynamic and photometric conditions. Artificial fog is an interesting alternative, but many studies simply use simulation, often validating their results by measurements in a mock-up scattering medium such as diluted milk in a transparent tank. Among the various laws which serve to model the particle size distribution of a natural dispersed medium [22], the modified Γ-distribution proposed by Deirmendjian [6] is the most popular to study fog [23, 24, 37]:

$$n(r) = A\, r^{\alpha}\, \mathrm{e}^{-b\, r^{\gamma}} \tag{2}$$

where $n(r)$ is the number of droplets per unit volume, r is the droplet radius and A, α, b and γ are the parameters which allow to fit the model to observations. Shettle and Fenn proposed a four-class fog typology based on this model [36]; the parameter sets to be used with (2) are presented in Tab. 1, and the particle size distributions are plotted in Fig. 1. Models 1 and 2 are characteristic of respectively heavy and moderate advection fogs, while models 3 and 4 are characteristic of respectively heavy and moderate radiation fogs, but Shettle and Fenn note that scaling the total particle number N is a relevant way to model other fog concentrations.

Fog	Model	A	α	b	γ	r_{m} (μm)	$N(\mathrm{cm}^{-3})$
Advection	1	0.027	3	0.3	1	10.0	20
	2	0.066	3	0.375	1	8.0	20
Radiation	3	2.373	6	1.5	1	4.0	100
	4	607.5	6	3.0	1	2.0	200

Table 1: Size distribution parameters of the fog granulometric models reported by Shettle and Fenn [36]: r_{m} is the mode radius, N is the total particle number, A, α, b and γ are the parameters of the modified Γ-law (2).

3 Light Scattering in Fog

3.1 Single scattering

What we perceive as light is actually a combination of monochromatic electromagnetic radiations with wavelengths between 380 and 780 nm, the visible spectrum of the human visual system. When passing through fog, these electromagnetic waves interact with airborne droplets, losing energy at every interaction. This extinction effect results from two phenomena:

- absorption, which transforms part of the luminous energy into thermal energy;
- scattering, which spreads the luminous energy from the incident direction into other directions.

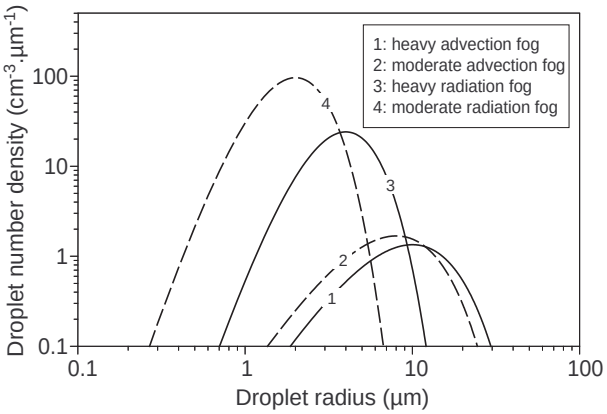

Figure 1: Fog droplet size distribution models reported by Shettle and Fenn [36].

3.1.1 Influent Parameters: Size and Wavelength

The relative importance of absorption in the extinction phenomenon depends on the chemical nature of the particle through the complex refractive index $m(\lambda)$ of the material it is made of, an index which depends on the wavelength λ. In the case of fog, formed exclusively of water droplets, it is roughly constant and equal to 1.33 for all wavelengths in the visible spectrum.

The spatial distribution of the energy scattered by a droplet depends on its radius, as well as on the wavelength. The ratio of the droplet radius to the wavelength determines the type of scattering which occurs:

- Rayleigh scattering is prominently caused by air molecules. It happens when the wavelength is much higher than the droplet radius ($r < \lambda/10$). The scattered luminous energy is then proportional to the fourth power of the wavelength. It causes the blue color of clear skies, but it is negligible in fog [22].

- Mie scattering concerns bigger particles such as water droplets. The spatial distribution of scattered energy then strongly depends on the refractive index $m(\lambda)$ and on its so called size parameter x:

$$x = 2\pi r/\lambda \tag{3}$$

3.1.2 Mie Scattering Theory

The importance of the extinction phenomenon is proportional to the section of space in which the wave interacts with the particle. This section, $C_{\text{ext}}(r)$, is called the extinction cross section. It is related to the particle cross section πr^2 by means of the factor $Q_{\text{ext}}(r)$, called the extinction efficiency:

$$C_{\text{ext}}(r) = Q_{\text{ext}}(r)\,\pi\,r^2 \tag{4}$$

The scattering efficiency $Q_{\text{sca}}(r)$ has an equivalent definition, allowing the characterization of scattering separately from absorption:

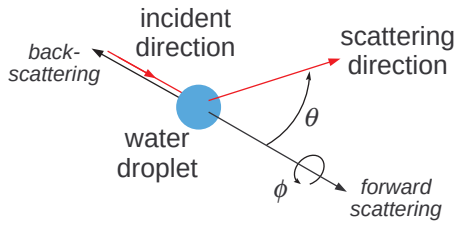

Figure 2: Light scattered by a water droplet.

The radiation scattered by the particle is characterized by its intensity, i.e. the energy flux per unit solid angle in the propagation direction. The scattered intensity thus depends on the scattering direction, defined by the angles θ and ϕ relative to the incident direction of the wave, as illustrated in Fig. 2.

The spatial distribution of scattered intensity is defined by the scattering diagram, more often called the phase function, $P(\theta, \phi)$. As fog droplets are spherical, their phase function is independent of angle ϕ, and only varies as a function of angle θ, or its cosine:

$$\mu = \cos\theta \tag{5}$$

Starting from Maxwell equations for electromagnetic waves, Lorenz expressed the efficiency factors for extinction, $Q_{\text{ext}}(r)$, and for scattering, $Q_{\text{sca}}(r)$, of a transparent sphere with a radius r, and the intensity scattered by this particle when it interacts with a planar monochromatic wave with a wavelength λ. His solution was later and independently generalized by Mie and by Debye. Here are the resulting equations [38]:

$$Q_{\text{ext}}(r) = \frac{2}{x^2}\sum_{n=1}^{\infty}(2n+1)\Re(a_n+b_n) \tag{6a}$$

$$Q_{\text{sca}}(r) = \frac{2}{x^2}\sum_{n=1}^{\infty}(2n+1)(|a_n|^2+|b_n|^2) \tag{6b}$$

$$S_1(\mu) = \sum_{n=1}^{\infty}\frac{2n+1}{n(n+1)}[a_n\pi_n(\mu)+b_n\tau_n(\mu)] \tag{6c}$$

$$S_2(\mu) = \sum_{n=1}^{\infty}\frac{2n+1}{n(n+1)}[a_n\tau_n(\mu)+b_n\pi_n(\mu)] \tag{6d}$$

S_1 and S_2 are the complex scattering amplitudes in both orthogonal incident polarization directions. The scattered intensity is proportional to the phase function:

$$P(r,\mu) = \frac{\lambda^2}{8\pi^2}\left(|S_1(\mu)|^2+|S_2(\mu)|^2\right) \tag{7}$$

Mie complex coefficients a_n and b_n depend on the size parameter and the refractive index. They are expressed in terms of primary and secondary Ricatti-Bessel functions and their derivatives. Function τ_n and π_n are expressed in terms of Legendre polynoms and their derivatives. The approximate number of terms of these series which need to be computed in order to obtain accurate results is of the same order as the size parameter x of the considered particle [40]. The full details of these calculations are reported in [39].

3.2 Multiple Scattering

3.2.1 Monodispersed Medium

Extinction is proportional to the concentration of particles on the path of the radiation. The consequent attenuation of luminous energy per unit distance is characterized by the extinction coefficient $K_{\text{ext}}(r)$. For a monodispersed medium formed of N particles of radius r per unit volume, $K_{\text{ext}}(r)$ is related to the extinction efficiency as follows:

$$K_{\text{ext}}(r) = NC_{\text{ext}}(r) = \pi N Q_{\text{ext}}(r) r^2 \tag{8}$$

The scattering coefficient $K_{\text{sca}}(r)$ is similarly related to the scattering efficiency.

3.2.2 Polydispersed Medium

A polydispersed medium can be characterized as an "equivalent" monodispersed medium, formed of one-sized particles which confer the same extinction and scattering properties to the equivalent medium as those of the actual medium. The equivalent extinction and scattering coefficients can be computed by convoluting the size-dependent extinction and scattering cross sections with the particle size distribution $n(r)$:

$$K_{\text{ext}} = \pi N \int_0^\infty Q_{\text{ext}}(r)\, n(r)\, r^2 \,\mathrm{d}\, r \tag{9a}$$

$$K_{\text{sca}} = \pi N \int_0^\infty Q_{\text{sca}}(r)\, n(r)\, r^2 \,\mathrm{d}\, r \tag{9b}$$

The equivalent phase function can be calculated in the same way:

$$P(\mu) = \pi N \int_0^\infty Q_{\text{ext}}(r)\, P(r,\mu)\, n(r)\, r^2 \,\mathrm{d}\, r \tag{10}$$

3.3 Fog Optical Properties

3.3.1 Extinction Coefficient

Thus, a monochromatic luminous wave undergoes extinction and scattering along its path in a dispersed medium, because of the particles which absorb and scatter its energy. The transmissivity T, i.e. the proportion of luminous energy transmitted along a path of length d, is given by Beer-Lambert law:

$$T = \mathrm{e}^{-K_{\text{ext}}\, d} \tag{11}$$

where K_{ext} is the extinction coefficient of the medium, expressed in m^{-1}.

The relative part played by scattering in this extinction phenomenon is characterized by the albedo a:

$$a = \frac{K_{\text{sca}}}{K_{\text{ext}}} \tag{12}$$

In the case of fog, in which the particles are water droplets, absorption of visible light is negligible. It follows that extinction is entirely caused by scattering. With an albedo equal to one, the extinction coefficient suffices to characterize the energy loss of light transmitted through fog. It is simply noted K:

$$K = K_{\text{ext}} \simeq K_{\text{sca}} \tag{13}$$

The extinction phenomenon along a path of length d may also be described by means of the optical depth τ:

$$\tau = Kd \tag{14}$$

3.3.2 Phase Function

In the visible light spectrum and in the size range of fog droplets, Mie scattering does not vary much with the wavelength. Therefore, fog optical properties can be calculated for a wavelength of 550 nm, where the human visual system is most sensitive in photopic conditions, and reasonably generalized to other visible wavelengths.

Because of the complexity of Mie equations, the phase function if often approximated by means of analytic expressions [13]. Nishita separated "hazy" and "murky" media, and proposed the following analytic expressions for their phase functions [2]:

$$P_{\text{hazy}}(\mu) = \frac{1}{2} + \frac{9}{2}\left(\frac{1+\mu}{2}\right)^8 \tag{15a}$$

$$P_{\text{murky}}(\mu) = \frac{1}{2} + \frac{33}{2}\left(\frac{1+\mu}{2}\right)^{32} \tag{15b}$$

Despite the fact that it was originally destined to the characterization of interstellar dust [21], the analytic phase function proposed by Henyey and Greenstein is very often used for scattering in the atmosphere:

$$P_{\text{HG}}(\mu, g) = \frac{1-g^2}{(1+g^2-2\,g\,\mu)^{3/2}} \tag{16}$$

The parameter $g \in]-1, 1[$ of this function is called the asymmetry factor:

$$g = \frac{1}{2}\int_{-1}^{1} P(\mu)\,\mu\,\mathrm{d}\mu \tag{17}$$

Its variations describe different scattering behaviors: when g is close to 1, scattering in the forward direction predominates; when g is close to -1, it is back-scattering (scattering in

the backward direction) which predominates; and when g is close to 0, scattering is almost isotropic. A simpler analytic form of Henyey-Greenstein phase function was proposed by Schlick [2]:

$$P_{\mathrm{S}}(\mu, k) = \frac{1 - k^2}{(1 - k\,\mu)^2} \tag{18}$$

where k is equivalent to the asymmetry factor g in (17). Schlick also showed that it was possible to produce phase functions resembling those of (15) or (16) by means of a linear combination of two of his phase functions:

$$P_{2\mathrm{S}}(\mu, \alpha, k, k') = \alpha\, P_{\mathrm{S}}(\mu, k) + (1 - \alpha)\, P_{\mathrm{S}}(\mu, k') \quad \text{where} \quad (\alpha, k, k') \in [0, 1] \times]-1, 1[^2 \tag{19}$$

Cornette and Shanks [5] proposed an analytic phase function which is similar to that of Henyey-Greenstein, only more physically-based and without the need for the extra weighting parameter of (19):

$$P_{\mathrm{CS}}(\mu, g) = \frac{3}{2}\,\frac{1 - g^2}{2 + g^2}\,\frac{1 + \mu^2}{(1 + g^2 - 2\,g\,\mu)^{3/2}} \tag{20}$$

Fig. 3 illustrates the limits of analytic models. Even with equal asymmetry factor, none of the listed expressions suitably accounts for the shape of the phase function computed for a given particle size distribution with Mie equations (6-7). The models tend to underestimate back-scattering, and to over-estimate scattering at intermediate angles, around 90°. The most important discrepancy lies in the forward-scattering "peak" caused by diffraction. Therefore, the Mie phase function should be preferred to analytic models when the granulometric data is available.

3.4 Visibility in Fog

Visibility is a complex notion, usually referring to the greatest distance at which an object can be detected or recognized. It depends on the geometric and photometric characteristics of the observed object and its background. In the presence of fog, visibility is affected on both geometric and photometric aspects because of the distance-dependent extinction effect.

Fog opacity is ordinarily characterized by means of the meteorological visibility V_{met}, defined as the visibility distance of a black object of "suitable" dimensions by day against the horizon sky [4]. However, meteorological visibility is a perceptual notion which cannot be easily measured. Fog opacity is more easily characterized by means of the meteorological optical range, defined as the length of the path in the atmosphere which is required to attenuate by 95% the luminous flux from a collimated light source [4]. This attenuation value was chosen because 5% is considered as the minimum visual contrast required to recognize an object against its background, in order to set an equivalence between the

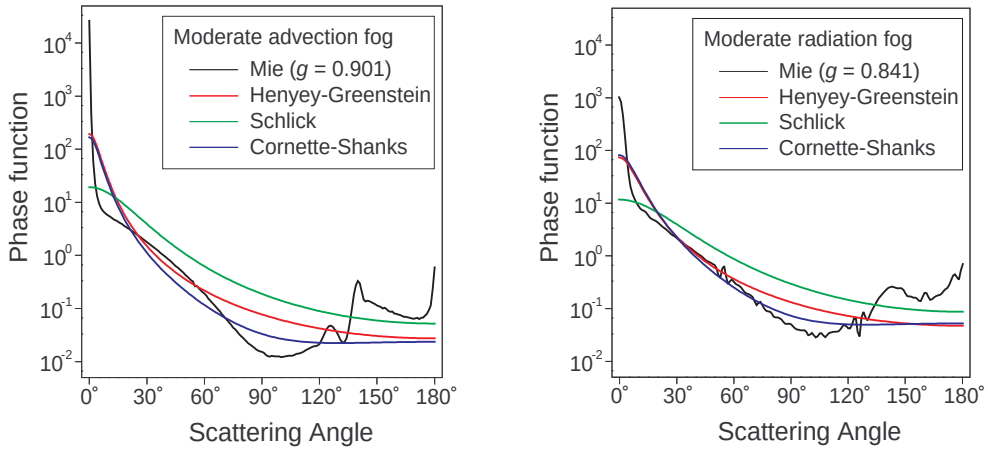

Figure 3: Comparison between Mie phase functions (computed from the fog granulometric models in Tab. 1) and different analytic models.

meteorological optical range and the meteorological visibility.

$$\begin{aligned} T &= \mathrm{e}^{-KV_{\mathrm{met}}} = 0.05 \\ V_{\mathrm{met}} &\simeq \frac{3}{K} \end{aligned} \tag{21}$$

Hence, meteorological visibility is in fact a more intuitive expression of the extinction coefficient K. Therefore, it is only an indication of fog opacity, and it should never be confused with the actual visual range of anything except a black object on the horizon sky in daytime.

4 Modeling Fog Effects on Vision

4.1 Fog Effects on the Visual Signal

4.1.1 Composition of the Visual Signal

As shown in Fig. 4, the image of the visual environment is formed by the luminance distribution which is projected into the eyes of an observer (or the aperture of a camera) by the elements of the observed scene. The luminance comes from the luminous energy emitted by the sky on the one hand, and by artificial light sources on the other hand. In normal visibility conditions, a small part of this energy reaches the observer directly, and the rest illuminates the surfaces throughout the scene. These surfaces then become secondary light sources, and a small part of the luminous energy is reflected toward the observer. Hence, the visual signal is composed of primary and secondary zones, depending whether light followed a single path or multiple paths to reach the observer.

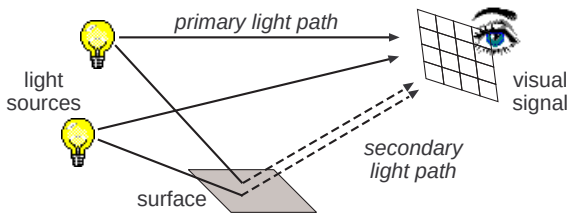

Figure 4: The visual signal is formed of the luminance which is either emitted by light sources (primary zones) or reflected by surfaces (secondary zones). Scattering by fog droplets occurs along light paths between the light sources, the surfaces and the observer.

4.1.2 Effects of Light Scattering

As seen in the previous section, light interacts with the airborne particles along its path. In fog, which is formed of water droplets with diameters ranging from several tenths to a few tens of microns, visible wavelengths are scattered without absorption. According to Mie theory, the directional distribution of scattered energy depends on the size of the droplets: the bigger droplets of advection or heavy radiation fog yield stronger forward scattering.

The main effect of fog on the visual signal is the attenuation of luminance caused by transmission through scattering droplets. This extinction effect is described by Beer-Lambert law (11), which results in an exponential attenuation of luminance with distance. It should be noted that extinction not only occurs between the elements in the scene and the observer, but also between the light sources and the surfaces.

$$L(d) = \mathrm{e}^{-Kd} L(0) \tag{22}$$

Since water droplets do not absorb visible light, scattered energy does not simply disappear: it is re-distributed throughout the scene. Part of it reaches the observer, causing further alterations to the visual signal. Scattered light thus produces two major visual effects, illustrated in Fig. 5.

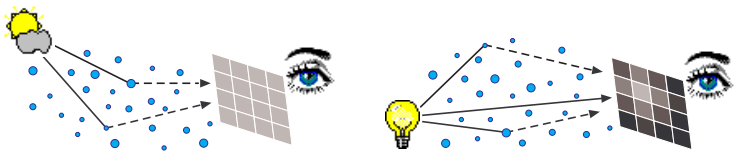

(a) Airlight. (b) Halo.

Figure 5: Airlight and halos are the two major alterations caused by scattered light in the visual environment of an observer in fog.

The first effect is caused by fog droplets scattering daylight toward the observer. According to Koschmieder theory of horizontal visibility, later generalized to slant visibility by Duntley (as reported in details by Middleton [28]), the resulting atmospheric veil L_{v} which is superimposed on the image of an object at a distance d is related to the luminance L_{f} of the fog at the horizon:

$$L_{\mathrm{v}} = \left(1 - \mathrm{e}^{-Kd}\right) L_{\mathrm{f}} \tag{23}$$

This effect is often referred to as airlight, and sometimes as path luminance. Koschmieder model provides a very simple and elegant expression for the luminance $L(d)$ of a non-luminous object at a distance d in daytime fog:

$$L(d) = \mathrm{e}^{-Kd} L(0) + \left(1 - \mathrm{e}^{-Kd}\right) L_{\mathrm{f}} \tag{24}$$

The luminance at close range $L(0)$ is generally called the intrinsic luminance.

The second effect is caused by fog droplets scattering the light they receive from artificial light sources toward the observer. According to the atmospheric modulation transfer function (MTF) theory [26], the resulting halo (or glow) effect is equivalent to the convolution of the image of the light source with the point spread function (PSF) of the fog. The PSF is the inverse Fourier transform of the MTF, which is distance-dependent. But using the analogy between a slab of fog and an optical filter, the MTF $M(K, d)$ of a homogeneous slab of fog of width d and extinction coefficient K can be derived from the MTF M of a slab of unit optical depth, called the frequency contrast operator (FCO) [9]:

$$M(K, d) = M^{Kd} \tag{25}$$

It should be noted that the FCO not only depends on the particle size distribution, as shown in Fig. 6, but also varies with the divergence of the considered light beam, because the halo comes essentially from light emitted outside of the observer's direction. Narrow beams (like those used in transmissometers) produce a negligible halo, especially in small droplet fogs.

4.2 Modeling Fog Visual Effects

4.2.1 Combining Extinction, Halos and Airlight

Based on the previous analysis of the mechanisms underlying visibility impairment, a unified model for the effects of fog on the visual signal can be proposed. The altered visual signal is computed in three steps: attenuation of secondary zones, convolution of primary zones and addition of airlight.

In the first step, the intrinsic luminance of visible surfaces must be decomposed in two parts: L_0 coming from daylight, and $L_{s\in[1,n]}$ issued by n artificial light sources present in the scene. The transmitted luminance of the secondary zones, L_{sec}, is computed by applying Beer-Lambert attenuation factor, first to the paths of lengths d_s from every light sources to

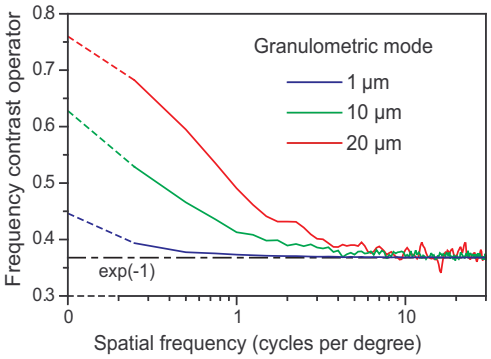

Figure 6: MTF of three types of fog with different droplet size distributions, computed by Monte-Carlo light tracing [9].

the surface, and then to the path of length d from the surface to the observer:

$$L_{\text{sec}} = \mathrm{e}^{-Kd}\left(L_0 + \sum_{s=1}^{n} \mathrm{e}^{-Kd_s} L_s\right) \tag{26}$$

In the second step, the intrinsic luminance L_s of each luminous object is "spread" onto the neighboring zones of the visual signal using the range dependent PSF of fog as a convolution kernel. The PSF is obtained by taking the inverse Fourier transform of the MTF of the slab of length d separating the object from the observer. The MTF is derived from the specified FCO M using (25). Thus, the transmitted luminance L_{pri} of primary zones can be expressed as follows:

$$L_{\text{pri}} = L_s * \mathcal{F}^{-1}\left\{M^{Kd}\right\} \tag{27}$$

In the final step, the path luminance, expressed in (23), is added to the result of the two previous steps, and yields the apparent luminance L perceived by the observer:

$$L = L_{\{\text{pri}|\text{sec}\}} + \left(1 - \mathrm{e}^{-Kd}\right) L_{\text{f}} \tag{28}$$

where $L_{\{\text{pri}|\text{sec}\}}$ is either L_{pri} for primary zones or L_{sec} for secondary zones in the visual signal, and L_{f} is the fog luminance.

4.2.2 Pros and Cons

Equations (26-28) constitute a unified photometric model of fog visual effects. It is in fact a generalization of Koschmieder law which accounts for artificial lighting, extending the field of applications to luminous objects and night-time or twilight situations.

However, very detailed photometric and geometric information is needed for its implementation. Moreover, the model retains some of the hypotheses and approximations of the theories on which it is based: in Koschmieder theory, fog is assumed to be homogeneous;

in the atmospheric MTF theory, light sources are assumed to emit isotropically toward the observer.

Also, the model does not deal with hidden light sources, though their halo may actually be visible. Finally, the scattered energy from the light sources is not taken into account in the intrinsic luminance of the surfaces. But getting past these limitations would require global illumination calculations, which are far less versatile than the presented image processing approach. And the model can be customized to overcome particular problems. For instance, when the observer is driving in fog, light from the headlamps of his motor-vehicle is scattered back into his field of vision as illustrated in Fig. 7: as the resulting back-scattered veil is independent of the scene, it can be pre-computed and then simply added to the foggy image of the scene [10, 11].

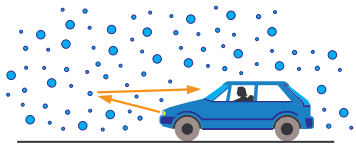

Figure 7: When driving in fog, light from the headlamps is back-scattered toward the driver, producing an additional veil in the driver's field of vision.

4.3 Implementation

4.3.1 Input

In order to use the proposed model to compute the bi-dimensional luminance distribution $L(i, j)$ seen by an observer looking at a scene in foggy weather conditions, detailed geometric and photometric information is needed. For each direction (i, j) in the visual field (which corresponds to a pixel in the image of the scene), the distance $d(i, j)$ of the pointed element in the scene, as well as its intrinsic luminance $L_0(i, j)$ as produced by ambient lighting, must be known. Furthermore, the distance $d_s(i, j)$ between the pointed element and each artificial light source s in the scene must be known, as well as the luminance $L_s(i, j)$ produced on the element by this light source. Hence, if n light sources are present in the scene, $n + 1$ luminance and range distributions are needed as input to the simulation, as described in Fig. 8.

The extinction coefficient K and the FCO M of the fog must also be specified in order to apply the proposed model, as well as the fog luminance L_f. The extinction coefficient is directly related to the meteorological visibility using (21). The FCO may be approximated from a model MTF [1] or from a model PSF [27]. As for fog luminance, Paulmier showed that it varies greatly with the altitude of the sun (and thus the hour of the day), the height of the fog layer and the type of fog, as well as the direction of observation with respect to the position of the sun [33].

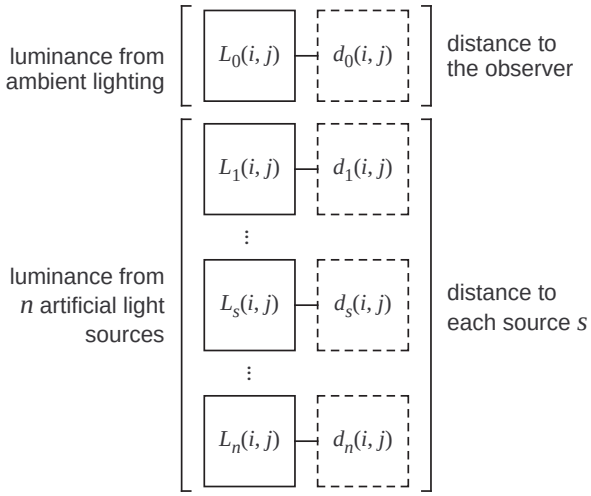

Figure 8: Detailed geometric and photometric description of the visual environment of an observer is needed to implement the photometric model of fog visual effects.

4.3.2 Semi-analytic Model

With the visual signal represented by the bidirectional luminance distribution $L(i,j)$ in the observer's field of vision, the model can be summarized in one equation, here including the back-scattered veil $L_b(i,j)$ mentioned earlier:

$$\begin{aligned} L(i,j) \;=\; & \left\{ \begin{array}{l} \mathrm{e}^{-Kd(i,j)} \left(L_0(i,j) + \sum_{s=1}^{n} \mathrm{e}^{-Kd_s(i,j)} L_s(i,j) \right) \\ L_s(i,j) * \mathcal{F}^{-1} \left\{ M^{Kd(i,j)} \right\} \end{array} \right. \\ & + \left(1 - \mathrm{e}^{-Kd(i,j)} \right) L_\mathrm{f} + L_b(i,j) \end{aligned} \tag{29}$$

4.3.3 Sample Results

To demonstrate the implemented model, it was applied to compute photometric images of a simple rural road scene in night-time and daytime foggy weather conditions. The 2D1/2 description of the driver's visual environment is presented in Fig. 9.

Radiation and advection types of fog were simulated. The computed luminance values were mapped to gray levels in order to produce the images presented in Fig. 10 for the night-time situation, and in Fig. 11 for the daytime situation.

It can be noted from the results that the relative importance of fog visual effects strongly depends on the lighting conditions (night or day) and on the microphysical nature of the fog (droplet size). The extinction effect yields the most important perturbations in the image of the scene. In night-time, particularly, every details vanish except the front- and rear-lamps of other vehicles, whereas they quickly fade into the distance in daytime because of the atmospheric veil. The halo effect around the light sources is much "smoother" with

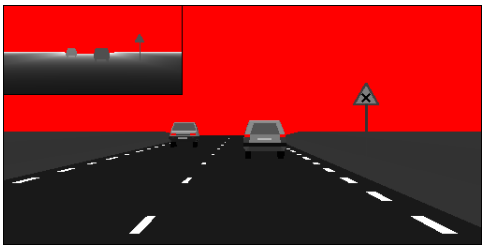

(a) Illumination from daylight.

(b) Illumination from the driver's vehicle headlights.

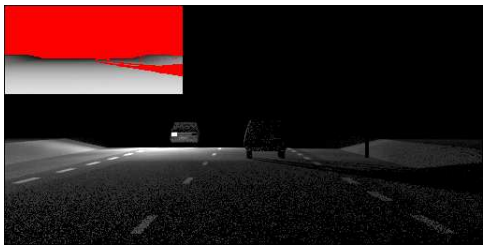

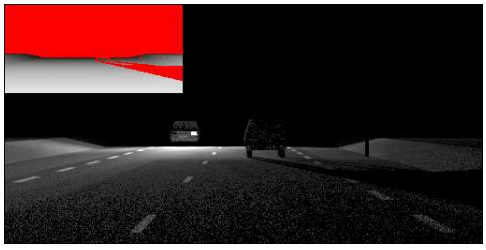

(c) Illumination from the oncoming vehicle headlights (at 150 m).

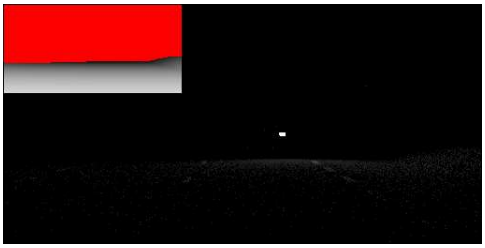

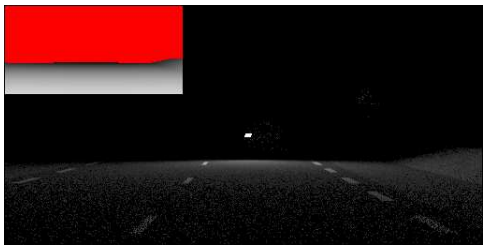

(d) Illumination from the rear-lights of the vehicle ahead (at 75 m).

Figure 9: Luminance and depth maps characterizing a rural road scene as described in Fig. 8, computed by Monte-Carlo light tracing [8]. Zones with undefinite depth from the observer (sky) or a light source (shadows) are shown in red.

(a) Without fog.

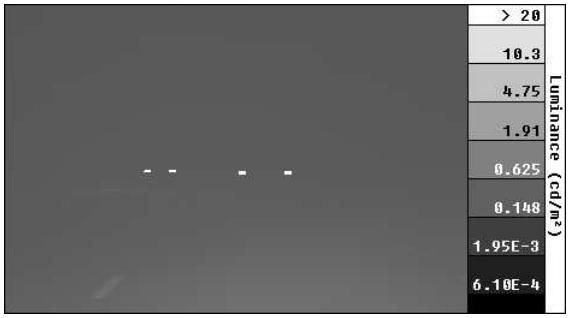

(b) Radiation fog.

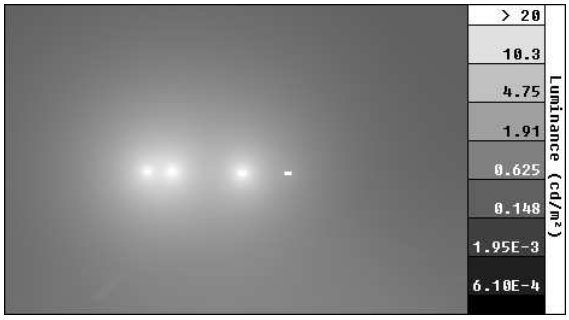

(c) Advection fog.

Figure 10: Computed luminance maps in the field of vision of a driver in a foggy rural scene during night-time (the meteorological visibility is 100 m).

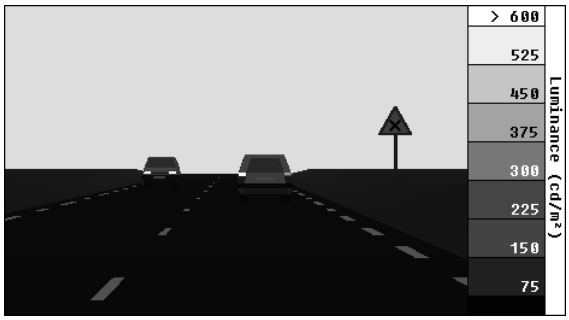

(a) Without fog.

(b) Radiation fog.

(c) Advection fog.

Figure 11: Computed luminance maps in the field of vision of a driver in a foggy rural scene during daytime (the meteorological visibility is 100 m, and the fog luminance is 500 cd.m^{-2}).

radiation fog, more like a veiling effect than with advection fog. As a consequence, the importance of the halos is greatly reduced by daytime airlight: they even seem negligible in radiation fog.

Although the images in Figs. 10&11 are only a tone-mapped representation of what the observer actually perceives, this example illustrates the complexity of fog effects on vision.

5 Application to the Validation of a Fog Observation Test Bench

5.1 Objectives

To improve road safety or the comfort of future vehicles, methods are being developed to detect the presence of fog and estimate the meteorological visibility distance through use of either in-vehicle [3, 19, 20] or roadside cameras [16, 17]. A major issue of this research is the quantitative evaluation of the methods [15]. To perform this task, the classical approach is to test the methods against a reference database [32]. The problem is to build the ground truth on the images in the database, usually by means of reference sensors. This involves some sort of visibilitymeter. Unfortunately, transmissometers are very expensive and scatterometers have some drawbacks, which make them unsuited to our needs [18].

To overcome this problem, we have thus proposed to build a fog observation test bench. This test bench is composed of a road track equipped with photometric targets which constitute a reference for assessing the meteorological visibility distance. They are passive targets for daytime and artificial light sources for nighttime, as already proposed in [25]. The fog model presented in the previous section is used to simulate the visual appearance of the test bench in foggy weather. We can then propose and test meteorological visibility distance estimation methods relying on the reference objects. It allows to predict the theoretical maximum accuracy of these methods, and to check if they are relevant to validate other methods which do not rely on any reference targets.

5.2 The Test Bench

For the daytime situation, our goal is to assess the contrast reduction in the reference targets, in order to estimate the value of the meteorological visibility distance. We equipped our test track in Versailles (France) with five large specific targets (cf. Fig. 12), located between 65 m and 200 m from the cameras onboard a vehicle stationed at a reference position (cf. Tab. 2a). For a maximum intrinsic contrast, we have designed black and white targets. To avoid aliasing effects, we have designed the targets so that they have the same apparent size in the images. An additional mobile target is used at a closer range when the fog is very dense.

For the nighttime situation, our goal is to assess the luminance reduction of artificial light sources. These light sources are set on top of the previous targets. Another mobile light source is set on the left side of the test track (see Fig. 12b). We use signal lights which ordinary serve in work zone areas. A typical configuration of the light sources in night tests is given in Tab. 2b.

Finally, based on the measurements given in Tab. 2, a virtual mockup of the test bench has been built. Fig. 13 shows this mockup in clear weather in full daylight. We have all the necessary geometric and photometric information concerning this mockup to simulate foggy weather on the test bench with the model presented previously.

(a)

Target index	1	2	3	4	5	6
Distance [m]	0-35	65.2	97.6	130.7	162.4	195
L [m]	0.5	1	1.5	2	2.5	3
t [m]	0.1	0.19	0.28	0.37	0.47	0.56

(b)

Target index	1'	2'	3'
Distance [m]	35	35-200	200

Table 2: (a) Index, distance and dimensions L, t (see Fig. 12c) of the different reference targets on the test bench for the daytime use. (b) Index and distance of the different light sources on the test bench for the nighttime use.

5.3 Daytime Situation

In this section, we first propose a process to measure the meteorological visibility distance using the black and white passive targets. Secondly, we check if this process is relevant by applying it on simulated images of the observation test bench in daytime fog.

5.3.1 Measurement Process

In daytime, with the sky as only light source, the model (29) simply comes down to Koschmieder law (24). Based on this equation, we can build two methods to estimate the meteorological visibility distance. The first method only uses the black part of the targets. The second one uses the black part as well as the white part of the targets.

- Using the black part of the targets

We consider the black part of two black targets located at distances d_1 and d_2 from the camera. We assume that they have a negligible intrinsic luminance ($L_\mathrm{b}(0) = 0$). According to (24), their apparent luminances are:

$$\left\{ \begin{array}{rcl} L_\mathrm{b}(d_1) & = & (1 - e^{-Kd_1})L_\mathrm{f} \\ L_\mathrm{b}(d_2) & = & (1 - e^{-Kd_2})L_\mathrm{f} \end{array} \right. \tag{30}$$

Taking the ratio $r_\mathrm{b} = \frac{L_\mathrm{b}(d_1)}{L_\mathrm{b}(d_2)}$ of these values, we obtain the following equation, which we need to solve for K:

$$r_\mathrm{b} = \frac{1 - e^{-Kd_2}}{1 - e^{-Kd_1}} \tag{31}$$

(a) (b)

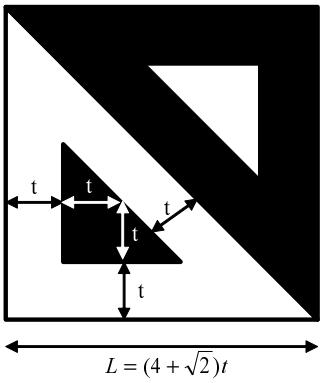

(c)

Figure 12: (a) Actual picture of the fog observation test bench dedicated to visibility measurement, taken in sunny weather conditions; (b) the mobile light source used in nighttime tests; (c) graphic design of the reference targets.

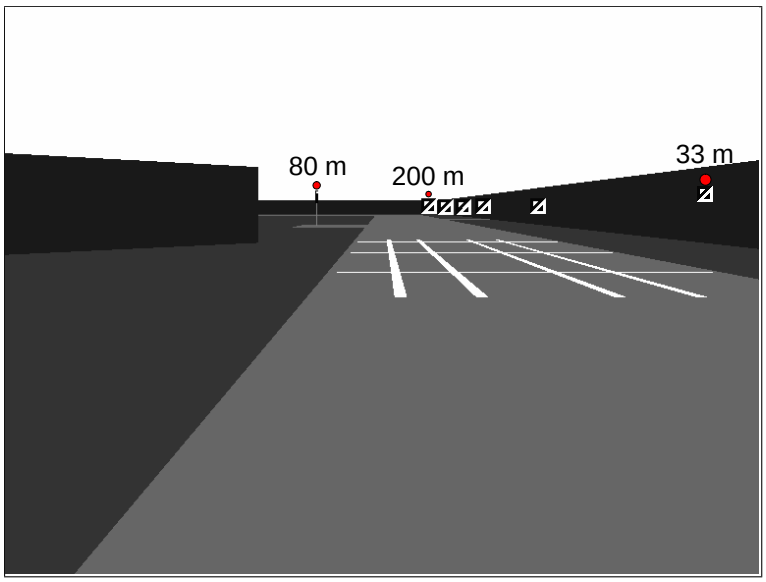

Figure 13: Image of the virtual mockup of the fog observation test bench. The signal lights are marked in red, and their relative positions are specified.

(31) admits analytical solutions for certain values of the ratio $\frac{d_2}{d_1}$. We deduce the value of the extinction coefficient K in different ways:

$$K = \begin{cases} -\frac{1}{d_1}\log\left(r_\mathrm{b}-1\right) & \text{if } d_2 = 2d_1 \\ -\frac{1}{d_1}\log\left(\frac{\sqrt{4r_\mathrm{b}-3}-1}{2}\right) & \text{if } d_2 = 3d_1 \\ -\frac{1}{d_1}\log\left(\frac{\left(r_\mathrm{b}-1\right)\left(\sqrt{r_\mathrm{b}+3}-\sqrt{r_\mathrm{b}-1}\right)^2}{4}\right) & \text{if } d_2 = \frac{3}{2}d_1 \end{cases} \tag{32}$$

- Using both black and white parts of the targets

An alternative technique consists in using the white and the black parts of the targets, whose apparent luminances $L_\mathrm{w}(d)$ and $L_\mathrm{b}(d)$ are given by (24):

$$\begin{cases} L_\mathrm{w}(d_1) - L_\mathrm{b}(d_1) &= e^{-Kd_1}L_\mathrm{w}(0) \\ L_\mathrm{w}(d_2) - L_\mathrm{b}(d_2) &= e^{-Kd_2}L_\mathrm{w}(0) \end{cases} \tag{33}$$

Again taking the ratio r_bw of these values, we have:

$$r_\mathrm{bw} = e^{-K(d_1-d_2)} \tag{34}$$

We deduce the value of extinction coefficient K:

$$K = \frac{1}{d_2-d_1}\log(r_\mathrm{bw}) \tag{35}$$

- Averaging the measurements

(32) and (35) each gives a single estimate of the meteorological visibility distance. By fusing the different estimates, we can have a more accurate overall estimate. In this aim, we must take into account the relative accuracy of each estimate. An estimation $\mathcal{V}(K)$ of the variance of K is thus associated with each formula (32) or (35). $\mathcal{V}(K)$ is expressed by:

$$\mathcal{V}(K) \approx \mathcal{V}_I \sum \left(\frac{\partial K}{\partial L_{\mathrm{b,w}}(d_{1,2})} \right)^2 \tag{36}$$

where $\mathcal{V}_I$ is the variance on the pixel value due to the digitalization of the pictures, assuming a Gaussian centered distribution with a standard deviation of $\frac{1}{2}$. From (21), we deduce the variance of V_{met}:

$$\mathcal{V}(V_{\mathrm{met}}) \approx \left(\frac{V_{\mathrm{met}}}{K} \right)^2 \mathcal{V}(K) \tag{37}$$

Assuming that the measurements are not correlated, these estimates are optimally averaged using the variances:

$$\widehat{V}_{\mathrm{met}} = \frac{\sum_i \frac{V_{\mathrm{met}_i}}{\mathcal{V}(V_{\mathrm{met}_i})}}{\sum_i \frac{1}{\mathcal{V}(V_{\mathrm{met}_i})}} \tag{38}$$

We deduce the variance of this estimator:

$$\mathcal{V}(\widehat{V}_{\mathrm{met}}) = \left(\sum_i \frac{1}{\mathcal{V}(V_{\mathrm{met}_i})} \right)^{-1} \tag{39}$$

5.3.2 Process Validation on Photometric Simulations

To check the measurement process presented in the previous paragraph, we must ensure that the equations are relevant for estimating the meteorological visibility distance. In this aim, using the model of fog effects on vision given in section 4.3.2, we simulated pictures of the virtual mockup of our test bench in daytime fog, for different values of V_{met}: 33 m, 66 m, 100 m, 133 m, 166 m and 200 m. These pictures are shown in Fig. 14.

Tab. 3a gives the values of $\widehat{V}_{\mathrm{met}}$ obtained thanks to averages of estimates (32). Tab. 3b gives the values of $\widehat{V}_{\mathrm{met}}$ obtained thanks to averages of (35). First, some results at the bottom of the tables are bad. The reason for that is the round-off caused by the digital nature of the simulated images. Thereafter, the logarithmic formula is more sensitive to the small intensity differences on the distant targets, than with the large intensity differences of closer targets. The estimated visibility distance is thus necessarily worst using the most distant targets. All these considerations are confirmed by the standard deviation values, which are given between brackets in Tab. 3. Second, the standard deviations in Tab. 3a are smaller than in Tab. 3b. Unfortunately, the method seems to be biased, because the estimated visibility distance is biased and always smaller than the ground truth. This may

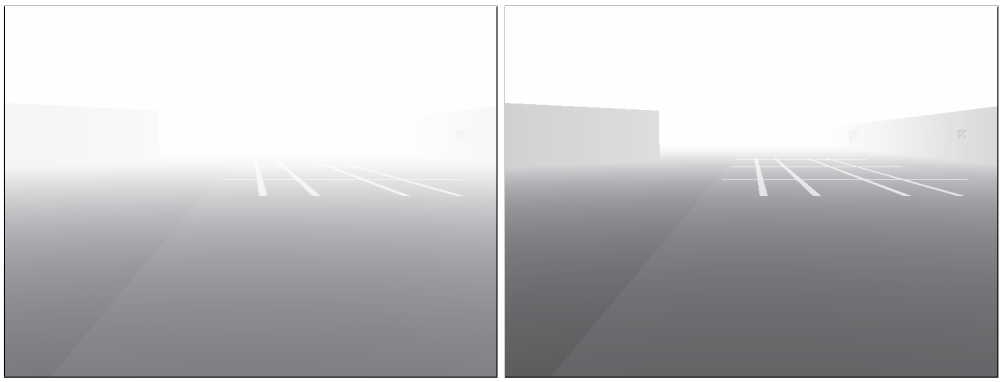

(a) $V_{\mathrm{met}} = 33$ m (b) $V_{\mathrm{met}} = 66$ m

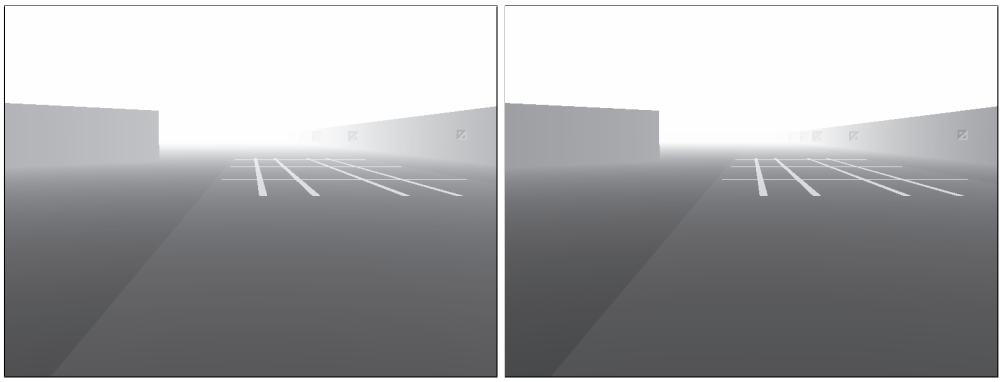

(c) $V_{\mathrm{met}} = 100$ m (d) $V_{\mathrm{met}} = 133$ m

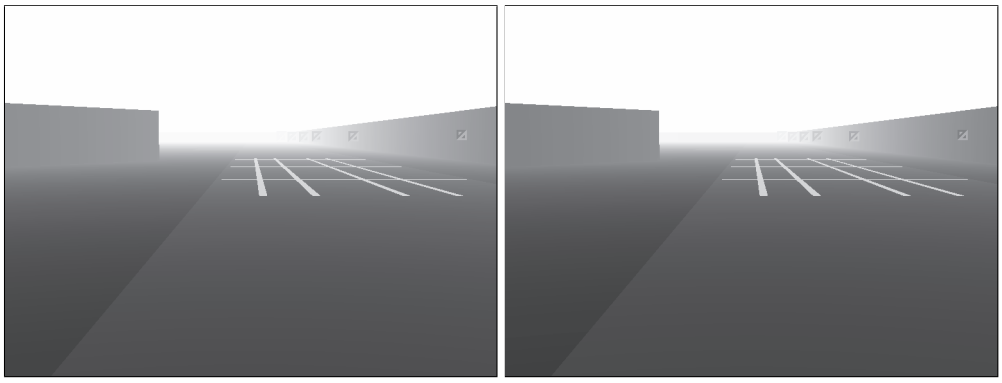

(e) $V_{\mathrm{met}} = 166$ m (f) $V_{\mathrm{met}} = 200$ m

Figure 14: Photometric simulations of the test bench in daytime fog for different meteorological visibility distances.

(a)

$\widehat{V}_{\mathrm{met}}(\sigma)$ **[m]**		V_{met} **[m]**				
		200	**166**	**133**	**100**	**66**
couple of targets	$1 \rightarrow 2$	172 (2.2)	144 (1.7)	119 (1.4)	92 (1.4)	61 (1)
	$1 \rightarrow 3$	183 (1.7)	151 (1.4)	124 (1.4)	95 (1)	-
	$2 \rightarrow 3$	199 (2.2)	161 (2)	132 (1.7)	100 (1.4)	-
	$2 \rightarrow 4$	197 (1.7)	162 (1.4)	132 (1.4)	-	-
	$2 \rightarrow 6$	198 (1.4)	-	-	-	-
	$3 \rightarrow 6$	197 (1.7)	-	-	-	-
	$4 \rightarrow 6$	199 (2)	-	-	-	-
	$\widehat{V}_{\mathrm{met}}$	194 (1)	155 (1)	126 (1)	95 (1)	61 (1)

(b)

$\widehat{V}_{\mathrm{met}}$ (σ) **[m]**		V_{met} **[m]**				
		200	**166**	**133**	**100**	**66**
couple of targets	$1 \rightarrow 2$	203 (3.7)	170 (3.5)	138 (3.2)	103 (3)	74 (3.3)
	$1 \rightarrow 3$	198 (3.2)	173 (3.2)	135 (3.2)	103 (3.3)	-
	$1 \rightarrow 4$	201 (3.3)	162 (3.3)	138 (3.6)	-	-
	$1 \rightarrow 5$	189 (3.6)	172 (3.9)	-	-	-
	$1 \rightarrow 6$	203 (4.1)	-	-	-	-
	$2 \rightarrow 3$	194 (4.6)	176 (4.8)	133 (4.5)	103 (4.8)	-
	$2 \rightarrow 4$	200 (4)	158 (4)	138 (4.5)	-	-
	$2 \rightarrow 5$	184 (4.1)	172 (4.5)	-	-	-
	$2 \rightarrow 6$	203 (4.6)	-	-	-	-
	$3 \rightarrow 4$	206 (6.2)	143 (5.4)	142 (6.8)	-	-
	$3 \rightarrow 5$	180 (5)	170 (5.6)	-	-	-
	$3 \rightarrow 6$	207 (5.5)	-	-	-	-
	$4 \rightarrow 5$	160(6.5)	210 (10.2)	-	-	-
	$4 \rightarrow 6$	207(6.8)	-	-	-	-
	$5 \rightarrow 6$	294 (14.6)	-	-	-	-
	$\widehat{V}_{\mathrm{met}}$	197 (2)	168 (2.2)	137 (2.4)	103 (2.6)	74 (3.3)

Table 3: Estimated meteorological visibility distance and standard deviation (between brackets) on simulated pictures using the reference targets and (a) average estimates (32) or (b) average estimates (35).

be due to the fact that the targets are not really black, as is assumed for establishing (32). In our simulations, we implemented a reflectance factor of 1% in order to stick to reality.

To confirm these statements, we plotted in Fig. 15 the estimated meteorological visibility distances with respect to the simulated meteorological visibility distances as well as the averaged estimates (32) and (35). In addition, linear regression lines are plotted using a black line for the averaged estimates and a dashed line for the ground truth. By looking at Fig. 15a, we have the confirmation that the method relying on the averaged estimates (32) is biased. However, the bias seems to be constant, which is a somehow interesting. By looking at Fig. 15b, it seems that the method relying on the averaged estimates (35) is relevant to estimate the meteorological visibility distance. Indeed, the regression line of the averaged estimates seems to merge with that of the ground truth for the highest meteorological visibility distances, where there are enough points to compute reliable averaged estimates.

Consequently, based on Tabs. 3a&b and Figs. 15a&b, it seems reasonable to only rely on the averages of (35) to compute the reference measurement $\widehat{V}_{\mathrm{met}}$. This reference measurement can then be used to assess the performances of methods which detect and estimate the fog density in daytime without any reference.

5.4 Nighttime Situation

In this section, we first propose a process to measure the meteorological visibility distance using artificial light sources. Second, we check if this process is relevant by applying it on simulated images of the observation test bench in nighttime fog.

5.4.1 Measurement Process

In nighttime, the light sources are the single visible objects in the test bench. Based on (29), the luminance of these light sources is given by:

$$L_{\mathrm{s}}(d) = L_s(0) * \mathcal{F}^{-1}\Big\{M^{Kd}\Big\} \tag{40}$$

This equation models both the luminance attenuation effect and the halo effect of night fog. We can split the model in two parts, where each part is related to each visual effect:

$$\begin{aligned} L_{\mathrm{s}}(d) &= L_{\mathrm{s}}(0) * \mathcal{F}^{-1}\Big\{M^{Kd} - e^{-Kd}\Big\} + L_{\mathrm{s}}(0) * \mathcal{F}^{-1}\Big\{e^{-Kd}\Big\} && \text{(41a)} \\ &= L_{\mathrm{s}}(0)e^{-Kd} + L_{\mathrm{s}}(0) * \mathcal{F}^{-1}\Big\{M^{Kd} - e^{-Kd}\Big\} && \text{(41b)} \end{aligned}$$

The first term of (41b) is related to the luminance attenuation effect, whereas the second term models the halo visual effect. Let us consider two targets located at two distinct distances d_1 and d_2. We can again take the ratio r_{s} of their luminances:

$$r_{\mathrm{s}} = \frac{L_{\mathrm{s}_1}(d_1)}{L_{\mathrm{s}_2}(d_2)} = \frac{L_{\mathrm{s}_1}(0)e^{-Kd_1} + L_{\mathrm{s}_1}(0) * \mathcal{F}^{-1}\Big\{M^{Kd_1} - e^{-Kd_1}\Big\}}{L_{\mathrm{s}_2}(0)e^{-Kd_2} + L_{\mathrm{s}_2}(0) * \mathcal{F}^{-1}\Big\{M^{Kd_2} - e^{-Kd_2}\Big\}} \tag{42}$$

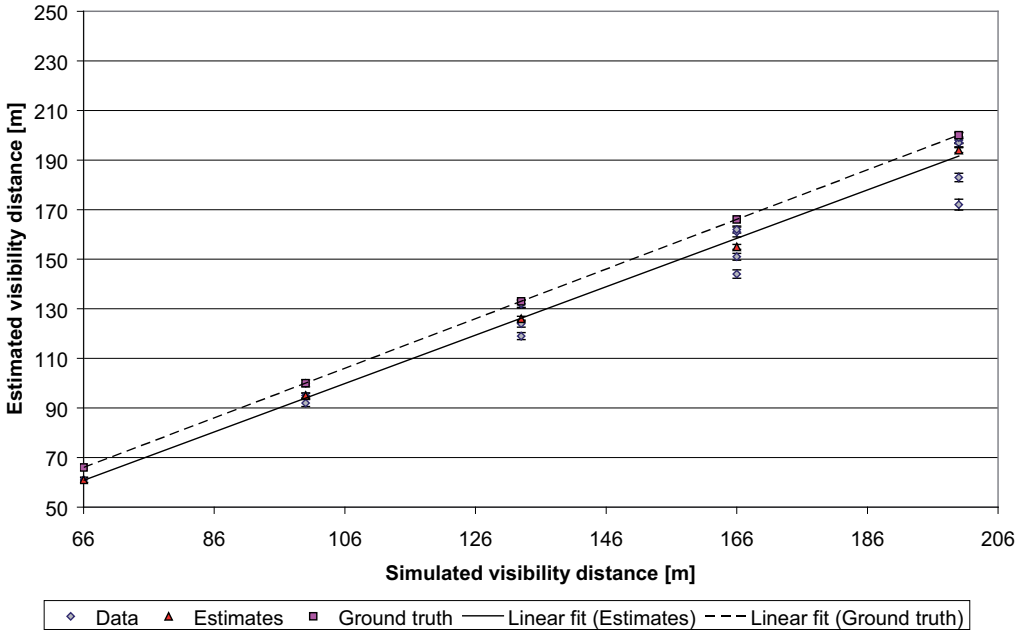

(a)

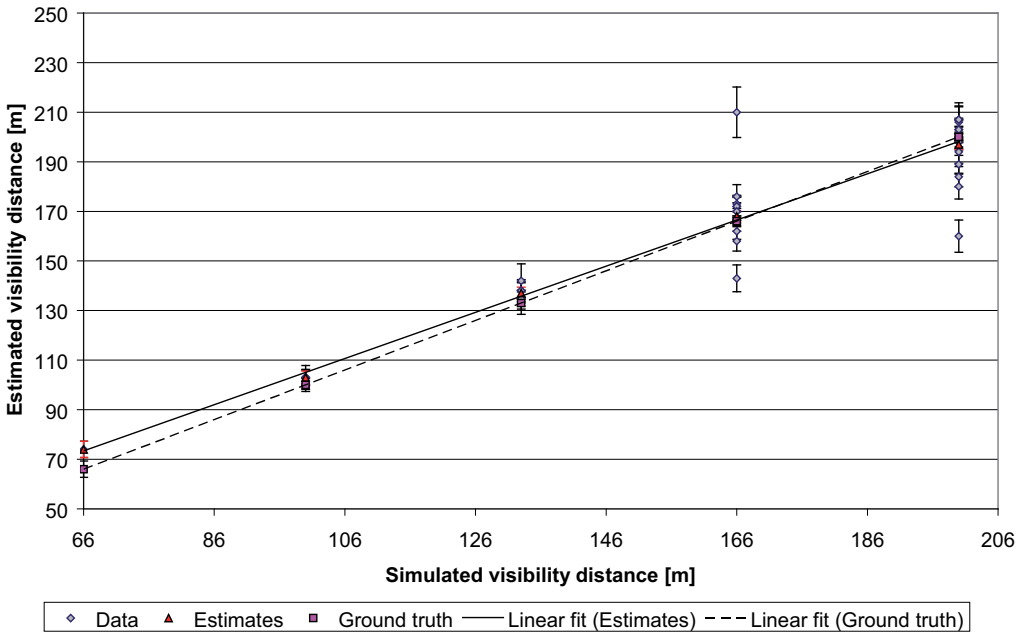

(b)

Figure 15: Plots of estimated vs. simulated meteorological visibility distances in daytime fog using the reference targets and (a) average estimates (32) or (b) average estimates (35). Linear regression lines are plotted using a black line for the averaged estimates and a dashed line for the ground truth.

In [30], the authors neglect the contribution of the halos to r_s. Based on this assumption, they compute the relative depth of light sources. This measurement process is rather simple since measuring the maximum luminance of the light sources is enough to compute fog density. We propose to use this assumption and thus (42) becomes:

$$r_{\mathrm{s}} = \frac{L_{\mathrm{s}_1}(0)}{L_{\mathrm{s}_2}(0)} e^{-K(d_2-d_1)} \tag{43}$$

Assuming that the light sources are identical, their intrinsic luminances are equal. We obtain finally:

$$K = \frac{1}{d_2 - d_1} \log(r_{\mathrm{s}}) \tag{44}$$

Since we have more than two light sources in the test bench, we can, like in section 5.3, fuse the different estimates obtained using (44). An estimation $\mathcal{V}(K)$ of the variance of K is thus associated with (44). $\mathcal{V}(K)$ is expressed by:

$$\mathcal{V}(K) \approx \mathcal{V}_I \sum \left(\frac{\partial K}{\partial L_{\mathrm{s}_{1,2}}(d_{1,2})} \right)^2 \tag{45}$$

where $\mathcal{V}_I$ is the variance on the pixel value due to the digitalization of the pictures, assuming a gaussian centered distribution with a standard deviation of $\frac{1}{2}$. From (21), we deduce the variance of V_{met}:

$$\mathcal{V}(V_{\mathrm{met}}) \approx \left(\frac{V_{\mathrm{met}}}{K} \right)^2 \mathcal{V}(K) \tag{46}$$

Assuming again that the measurements are not correlated, these estimates are optimally averaged using the variances:

$$\widehat{V}_{\mathrm{met}} = \frac{\sum_i \frac{V_{\mathrm{met}_i}}{\mathcal{V}(V_{\mathrm{met}_i})}}{\sum_i \frac{1}{\mathcal{V}(V_{\mathrm{met}_i})}} \tag{47}$$

The variance of this estimator is again:

$$\mathcal{V}(\widehat{V}_{\mathrm{met}}) = \left(\sum_i \frac{1}{\mathcal{V}(V_{\mathrm{met}_i})} \right)^{-1} \tag{48}$$

5.4.2 Process Validation on Photometric Simulations

In the previous section, we assume that the halos can be neglected to compute the meteorological visibility distance. In this section, we propose to check if this assumption is valid. Based on the model of fog effects on vision given in section 4.3.2, we have performed photometrical simulations of the test bench in nighttime. We simulated different meteorological visibility distances (33 m, 66 m, 100 m, 133 m, 166 m and 200 m) and droplet size distributions using moderate advection and radiation fogs from Tab. 1. Some samples of simulated pictures are shown in Fig. 16. One can see that the visual appearance of the light

sources differ even if the meteorological visibility distance is the same, as it was already mentioned in section 4.3.3. The halos seem to be more intense for advection fog than for radiation fog. One can see also that the most distant light source (index 3') is no longer visible for very low meteorological visibility distances. The intermediate source (index 2') is also barely visible.

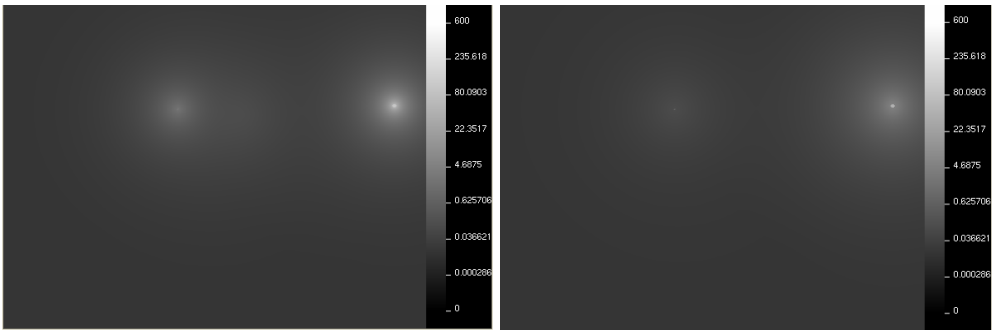

(a) $V_{\mathrm{met}} = 33$ m G2

(b) $V_{\mathrm{met}} = 33$ m G4

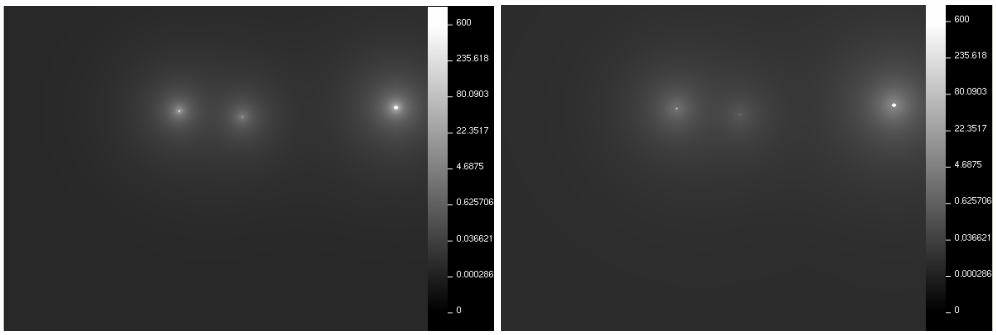

(c) $V_{\mathrm{met}} = 200$ m G2

(d) $V_{\mathrm{met}} = 200$ m G4

Figure 16: Samples of the photometric simulations of the test bench in nighttime fog for different meteorological visibility distances and different droplet size distributions (G2 moderate advection fog; G4 moderate radiation fog).

Tab. 4a gives the values of $\widehat{V}_{\mathrm{met}}$ obtained thanks to averages of estimates (44) in advection fog (denoted G2). Tab. 4b gives the values of $\widehat{V}_{\mathrm{met}}$ obtained thanks to averages of estimates (44) in radiation fog (denoted G4).

First, we can see that the variances of the averaged estimates are bigger that those obtained in daytime. This can be related to the fact that fog effects are more complex in nighttime than in daytime. Indeed, the model used in nighttime is semi-analytic whereas in daytime it is completely analytic. The non-analytic part of the model is noise sensitive,

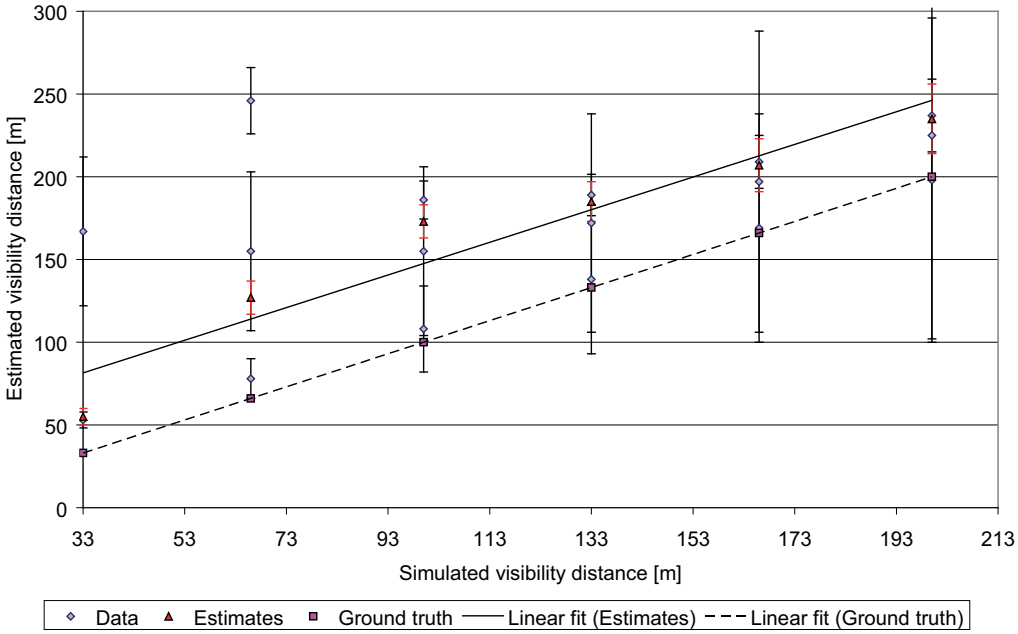

(a)

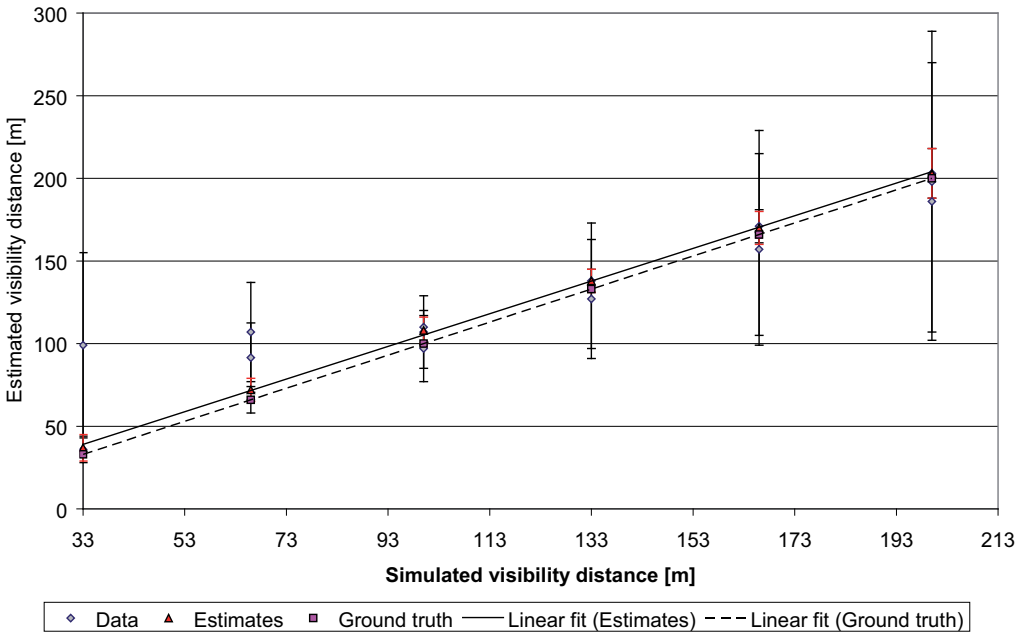

(b)

Figure 17: Plots of estimated vs. simulated meteorological visibility distances in nighttime (a) advection and (b) radiation fog using the artificial light sources and average estimates (44). Linear regression lines are plotted using a black line for the averaged estimates and a dashed line for the ground truth.

(a)

$\widehat{V}_{\mathrm{met}}(\sigma)$ **[m]**		V_{met} **[m]**					
		200	**166**	**133**	**100**	**66**	**33**
couple of targets	$1' \to 2'$	198 (98)	169 (69)	138 (45)	108 (26)	78 (12)	53 (4.8)
	$1' \to 3'$	225 (123)	197 (91)	172 (66)	155 (51)	155 (48)	167 (45)
	$2' \to 3'$	237 (22)	209 (16)	189 (12.5)	186 (11.5)	246 (20)	846 (389)
	$\widehat{V}_{\mathrm{met}}$	235 (21)	207 (16)	185 (12)	173 (10)	127 (10)	55 (5)

(b)

$\widehat{V}_{\mathrm{met}}(\sigma)$ **[m]**		V_{met} **[m]**					
		200	**166**	**133**	**100**	**66**	**33**
couple of targets	$1' \to 2'$	186 (84)	157 (58)	127 (36)	97 (20)	66 (8)	36 (8)
	$1' \to 3'$	198 (91)	167 (62)	135 (38)	107 (22)	91.5 (21)	99 (56)
	$2' \to 3'$	203 (15)	171 (10)	138 (7)	110 (10)	107 (30)	294 (699)
	$\widehat{V}_{\mathrm{met}}$	203 (15)	170 (10)	138 (7)	108 (8)	72 (7)	37 (8)

Table 4: Estimated meteorological visibility distance and standard deviations (between brackets) on simulated pictures using the artificial light sources and (44) in (a) moderate advection fog and (b) moderate radiation fog.

which partly explains the higher variances of the measurements.

Second, we can see that the averaged estimates are far from the ground truth in advection fog (see Tab. 4a), whereas they are quite close to the ground truth in radiation fog (see Tab. 4b). This can be directly related to the droplet size distributions. For the moment, we can state that the halo effect cannot be neglected to estimate the meteorological visibility distance. (44) is thus questionable.

To go further in the details, we plotted in Fig. 17 the estimated meteorological visibility distances with respect to the simulated meteorological visibility distances as well as the averaged estimates (44). In addition, linear regression lines are plotted using a black line for the averaged estimates and a dashed line for the ground truth. These plots are given for advection fog in Fig. 17a, as well as for radiation fog in Fig. 17b. By looking at these plots, we have the confirmation that the proposed measurement process is biased, since it overestimates the meteorological visibility distance. However, the bias seems to be constant thanks to the proposed averaging process, which is rather interesting. Indeed, it provides a practical solution to correct the bias. In this aim, with approximate knowledge of the granulometry of the fog, i.e. the type of fog, we can correct the bias to get a better estimate $\widehat{V}_{\mathrm{met}}$ of the meteorological visibility distance. We can also ignore this bias if radiation fog is encountered.

In the future, it would be relevant to not only use the luminance attenuation of the light sources, but also to use the shape of the halos to estimate the granulometry of the fog and thus correct the bias. [27, 31] are good examples of such a process, but for the fact that they both rely on the Henyey-Greenstein phase function (16), which we saw was not the best model for fog.

5.5 Partial Assessment

In this section, we have shown an application of the proposed model of fog effects on vision to the validation of a fog observation test bench. First, we have described the test bench, in particular the photometric references which are used. Second, we have tackled the daytime fog situation. It has been shown that using both black and white parts of the passive targets leads to a good estimation of the meteorological visibility distance. Third, we have tackled the nighttime fog situation. It has been shown that the contribution of halos to the visual appearance of light sources cannot be neglected to estimate the meteorological visibility distance. Indeed, it leads to underestimate the fog density. However, in the specific case of radiation fog, which is the most typical type of fog, the proposed measurement process provides quite good results.

6 Conclusion

After examining the microphysical and optical characteristics of fog, and the resulting effects on the visual environment perceived by an observer or recorded by a camera, one thing at least appears obvious: there is more to fog than just the meteorological visibility distance. Indeed, we found that there are different kinds of fog, radiation and advection fogs being the most common, which appear and dissipate in different places and at different times. And we saw that these fogs are formed of water droplets which come in different sizes, between several tenths of a micron for radiation fog to several microns for advection fog. Then we showed that each droplet scatters visible light in an angular distribution which depends on its size, bigger droplets favoring the forward scattering. And when light travels through fog, scattered by multiple droplets along the way, it is exponentially attenuated with distance (Beer-Lambert law). This phenomenon is characterized by the extinction coefficient, which describes fog density. The meteorological visibility distance was conventionally defined as a more intuitive way to express the extinction coefficient. But extinction does not entirely describe the visual effects of fog. Some of the light scattered along light paths reaches the field of vision, adding two kinds of veils. The most obvious is the airlight, caused by the scattering of daylight: it adds a distance dependent veiling luminance to the visual signal (Koschmieder law). But artificial light sources also contribute some scattered light to the visual signal, only in a more localized way, under the form of halos which strongly depend on the type of fog because of the influence of droplet size on light scattering.

When investigating visual perception in fog, or when designing solutions to detect, measure or remove fog in digital images, one should not forget that extinction, airlight and halos happen simultaneously, with different relative effects. This is what led us to propose a unified model of fog effects on vision, applicable for both dark and luminous objects, under both daytime and night-time, as well as in twilight. It is a semi-analytic model because of the halo effect, modeled as a distance dependent PSF. Its implementation requires detailed geometric and photometric knowledge on the scene. But despite its limitations, it offers a convenient and versatile tool to predict fog effects, or to extract information about the scene

or the fog by image processing.

To demonstrate the benefit of using the model, we show how it helped us validate a fog observation test bench for camera-based fog monitoring applications. The test bench consists of black and white targets for daytime fog and light sources for nighttime fog. Several targets are installed at different distances from a reference observation point along a test track. A virtual mockup of this test bench was built, and the model of fog effects on vision was applied to compute digital images of the scene in different daytime and nighttime visibility conditions (with radiation and advection fog, and meteorological visibility distances between 30 m and 200 m). Different methods were tested to estimate the meteorological visibility distance from the reference objects in the images, and the estimated values were compared to the simulated values. It allowed us to prove that evaluating fog density directly in the images, using the reference objects, was a valid alternative to the deployment of an expensive visibilitymeter. It also allowed to reveal that neglecting the halo effect may lead to an underestimation of the meteorological visibility distance in advection fog.

References

[1] L.R. Bissonnette. Imaging through the atmosphere: Practical instrumentation-based theory and verification of aerosol modulation transfer function: Comment. *Journal of the Optical Society of America A*, 11(3):1175–1179, March 1993.

[2] P. Blasi, B. Le Saëc, and C. Schlick. A rendering algorithm for discrete volume density objects. In *Rendering Techniques '93*, pages 201–210, Vienna, 1993. Springer-Verlag.

[3] C. Boussard, N. Hautière, and B. d'Andréa Novel. Vehicle dynamics estimation for camera-based visibility range estimation. In *Proceedings of the IEEE/RSJ International Conference on Intelligent RObots and Systems, Nice France*, September 2008.

[4] CIE. *International Lighting Vocabulary*. Number 17.4. 1987.

[5] W. M Cornette and J. G. Shanks. Physically reasonable analytic expression forthe single-scattering phase function. *Applied Optics*, 31(16):3152–3160, 1992.

[6] D. Deirmendjian. *Electromagnetic Scattering on Spherical Polydispersions*. American Elsevier, New York, 1969.

[7] A. S. Drofa and I. L. Katsev. Certain problems of seeing through clouds and fogs. *Meteorologiya i Gidrologiya*, 11:101–109, 1981.

[8] E. Dumont. Semi-monte-carlo light tracing for the study of road visibility in fog. In *Monte Carlo and Quasi-Monte Carlo Methods 1998*, pages 177–187, Berlin, 1999. Springer-Verlag.

[9] E. Dumont. *Caractérisation, modélisation et simulation des effets visuels du brouillard pour l'usager de la route*. PhD thesis, Université Paris V, Novembre 2002.

[10] E. Dumont and V. Cavallo. Extended photometric model of fog effects on road vision. *Transportation Research Record*, (1862):77–81, 2004.

[11] E. Dumont, G. Paulmier, P. Lecocq, and A. Kemeny. Assessment of the simulation of low-beams backscattering in fog. In *Proceedings of the 6th International Symposium on Automotive Lighting (Darmstadt, Germany, September 27-28, 2005)*, pages 880–889, 2005.

[12] T. Elias, M. Haeffelin, P. Drobinski, J.-C. Dupont, C. Fesquet, H. Holin, E. Dupont, L. Musson-Genon, T. Bergot, and L. Gomes. The fog life cycle described by the parisfog field experiment. *Geophysical Research Abstracts*, 10, 2008.

[13] Andrew S. Glassner. *Principles of Digital Image Synthesis*. Morgan Kaufmann Pub., San Francisco, CA, 1995.

[14] D. Guédalia and T. Bergot. Premiers résultats de la campagne «lille 88» d'étude du brouillard. *La Météorologie*, 42:11–20, 1992.

[15] N. Hautière, D. Aubert, E. Dumont, and J.-P. Tarel. Experimental validation of dedicated methods to in-vehicle estimation of the atmospheric visibility distance. *IEEE Transactions on Instrumentation and Measurement*, 27(10), October 2008.

[16] N. Hautière, E. Bigorgne, and D. Aubert. Daytime visibility range monitoring through use of a roadside camera. In *Proceedings of the IEEE Intelligent Vehicles Symposium, Eindhoven, The Netherlands*, June 2008.

[17] N. Hautière, E. Bigorgne, J. Bossu, and D. Aubert. Meteorological conditions processing for vision-based traffic monitoring. In *IEEE International Workshop on Visual Surveillance, Marseille, France*, October 2008.

[18] N. Hautière, R. Labayrade, and D. Aubert. Estimation of the visibility distance by stereovision: a generic approach. *IEICE Transactions on Information and Systems*, E89-D(7):2084–2091, July 2006.

[19] N. Hautière, R. Labayrade, and D. Aubert. Real-time disparity contrast combination for onboard estimation of the visibility distance. *IEEE Transactions on Intelligent Transportation Systems*, 7(2):201–212, June 2006.

[20] N. Hautière, J.-P. Tarel, J. Lavenant, and D. Aubert. Automatic fog detection and estimation of visibility distance through use of an onboard camera. *Machine Vision and Applications Journal*, 17(1):8–20, April 2006.

[21] L. C. Henyey and J. L. Greenstein. Diffuse radiation in the galaxy. *Astrophysical Journal*, 93:70–83, 1941.

[22] Rudolf B. Husar. Physics and chemestry of atmospheric aerosols. A course given at the University of Stockholm (Department of Meteorology), fall semester 1976.

[23] Alex A. Kokhanovsky. *Optics of Light Scattering Media - Problems and Solutions*. John Wiley & Sons, 1999.

[24] Christos Kontogeorgakis. Millimeter through visible frequency waves through aerosols -particle modeling, reflectivity and attenuation. Master's thesis, Virginia Polytechnic Institute and State University, Blacksburg, VA, 1997.

[25] T. M. Kwon. Atmospheric visibility measurements using video cameras: Relative visibility. Technical report, University of Minnesota Duluth, July 2004.

[26] R.F. Lutomirsky. Atmospheric degradation of electrooptical system performance. *Applied Optics*, 17(24):3915–3921, 1978.

[27] S. Metari and F. Deschênes. A new convolution kernel for atmospheric point spread function applied to computer vision. In *Proceedings of the IEEE International Conference on Computer Vision, Rio de Janeiro, Brazil*, October 2007.

[28] W.E.K. Middleton. *Vision through the atmosphere*. University of Toronto Press, 1952.

[29] N. Nameda. Fog modulation transfer function and signal lighting. *Lighting Research & Technology*, 24(2):103–106, 1992.

[30] S. G. Narasimhan and S. K. Nayar. Vision and the atmosphere. *International Journal of Computer Vision*, 48(3):233–254, July-August 2002.

[31] S. G. Narasimhan and S. K. Nayar. Shedding light on the weather. In *Proceedings of the IEEE Computer Society Conference on Computer Vision and Pattern Recognition, Madison, Wisconsin, USA*, June 2003.

[32] S. G. Narasimhan, C. Wang, and S. K. Nayar. All the images of an outdoor scene. In *Proceedings of the European Conference on Computer Vision, Copenhagen, Denmark*, May 2002.

[33] Giselle Paulmier. Fog luminance evaluation in daytime. *Transportation Research Record*, (1862):82–88, 2004.

[34] Frederic Pérez, Xavier Pueyo, and François-Xavier Sillion. Global illumination techniques for the simulation of participating media. In *Rendering Techniques '97*, pages 309–320, New-York, June 1997. Springer-Verlag.

[35] Zi-qin Sang, Ming-yue Ding, and Tian-xu Zhang. Imaging for outdoor scene in rain and fog. *Acta Electronica Sinica*, 28(3):131–133, March 2000.

[36] Eric P. Shettle and Robert W. Fenn. Models for the aerosols of the lower atmosphere and the effectsof humidity variations on their optical properties. AFGL-TR 79-0214, Air Force Geophysics Laboratory, Hanscom Air Force Base, MA, 1979.

[37] Robert E. Turner and Peter F. Lambeck. Natural and artificial illumination in optically thick atmospheres. Final report 108300-4-F, Environment Research Institute of Michigan, Ann Arbor, MI, 1975.

[38] Hendrik C. van de Hulst. *Scattering by Small Particles*. Structure of matter. Dover, New York, 1981.

[39] Warren J. Wiscombe. Mie scattering calculations: Advances in technique and fast,vector-speed computer codes. NCAR/TN 140+STR, National Center for Atmospheric Research, Boulder, CO, June 1979. Edited/revised August 1996.

[40] Warren J. Wiscombe. Improved mie scattering algorithms. *Applied Optics*, 19(9):1505–1509, May 1980.